crystals

MDPI

Article

Surface Crystallization of Barium Fresnoite Glass: Annealing Atmosphere, Crystal Morphology and Orientation

Franziska Scheffler [1,*], Mirjam Fleck [1], Richard Busch [2], Santiago Casado [3], Enrico Gnecco [4], Christopher Tielemann [5], Delia S. Brauer [1] and Ralf Müller [5]

[1] Otto-Schott-Institut für Materialforschung, Friedrich-Schiller-Universität, Fraunhoferstr. 6, 07743 Jena, Germany
[2] Fraunhofer-Institut für Mikrostruktur von Werkstoffen und Systemen, Walter-Hülse-Str. 1, 06120 Halle, Germany
[3] Facultad de Ciencia e Ingeniería en Alimentos y Biotecnología, Universidad Técnica de Ambato, Avda. Los Chasquis y río Payamino s/n, Ambato 180207, Ecuador
[4] Marian Smoluchowski Institute of Physics, Jagiellonian University, Lojasiewicza 11, 30-348 Krakow, Poland
[5] Bundesanstalt für Materialforschung und -Prüfung (BAM), Richard-Willstätter-Str. 11, 12489 Berlin, Germany
* Correspondence: franzi.scheffler@uni-jena.de

Abstract: Controlled oriented crystallization of glass surfaces is desired for high precision applications, since the uppermost crystal layer significantly influences the properties of the material. In contrast to previous studies, the data presented here deal with separated crystals growing at defect-free surfaces in four atmospheres with different degrees of humidity (ambient/dry air, argon and vacuum). A glass with the composition 2 BaO–TiO_2–2.75 SiO_2 was heat-treated at 825 °C until fresnoite ($Ba_2TiSi_2O_8$) grew to a significant size. The crystal growth rate is found to increase with increasing humidity. The morphology of the crystals changes from highly distorted dendrites in the driest atmosphere (vacuum) to circular/spear-head-shaped crystals in the wettest atmosphere (ambient air), which we attribute to a decrease in viscosity of the glass surface due to water uptake. The least distorted crystals appear in the form of depressions of up to 6 µm. This has an influence on the observed crystal orientation, as measured by electron backscatter diffraction (EBSD). The pulled-in crystals change the orientation during growth relative to the flat glass surface due to an enrichment in SiO_2 at the crystal fronts. This confirms that the orientation of crystals is not fixed following nucleation.

Keywords: fresnoite; glass-ceramic; surface crystallization; crystal growth; crystal morphology; surface topography; crystal orientation; EBSD; atmosphere

Citation: Scheffler, F.; Fleck, M.; Busch, R.; Casado, S.; Gnecco, E.; Tielemann, C.; Brauer, D.S.; Müller, R. Surface Crystallization of Barium Fresnoite Glass: Annealing Atmosphere, Crystal Morphology and Orientation. *Crystals* **2023**, *13*, 475. https://doi.org/10.3390/cryst13030475

Academic Editors: Weiwei Tang and Josep Lluís Tamarit

Received: 2 February 2023
Revised: 27 February 2023
Accepted: 4 March 2023
Published: 9 March 2023

1. Introduction

Owing to their pyroelectric [1–3], piezoelectric [1,2,4,5] as well as non-linear optical properties [6–8], fresnoite glass-ceramics containing oriented barium fresnoite ($Ba_2TiSi_2O_8$, BTS) crystals are particularly interesting for a variety of applications. As fresnoite crystals are not ferroelectric [9,10], a modification of the existing polar structure, e.g., by an external electric field, is not possible. As a result, a polar structure is permanently present once the glass-ceramic structure is formed. This allows for specialized applications such as in the field of piezoelectric components, such as sensors for high-temperature and high-frequency industrial devices, or optical items such as frequency doublers [6] and pyroelectric parts [11].

In the past, various methods such as electrochemically induced nucleation from Pt wires [5,12–15], laser patterning [16,17] or, most frequently [11], surface-induced crystallization [8] were used to prepare fresnoite glass-ceramics with oriented crystals. As the perpendicular orientation of the crystals nucleated at the glass surface is primarily a result

of growth selection, the oriented crystal layer begins a few micrometers below the surface [18]. The uppermost surface layer is, thus, often characterized by less or even randomly oriented crystals [11]. Owing to the negative impact of this effect on the properties of the glass-ceramic, a minimization of that uppermost layer is desirable. This minimization can be achieved using a temperature gradient [1,19], by dusting with foreign particles [20], or surface damage with fresnoite crystal powders in an ultrasonic bath [8]. The latter methods increase the degree of surface crystal orientation, because surface roughness and solid foreign particles provide active sites for nucleation [21,22].

Nevertheless, preferred crystal orientation can even be found at the uppermost surface layer when the preferential orientation of the crystals is not likely to be the result of growth selection [23]. This is supported by the fact that the orientation of the initial surface crystals is not identical to the orientation of later occurring crystal growth selection. Evidence for this is provided by electron backscatter diffraction (EBSD) measurements, which gather data at a depth of <60 nm [24] and are, thus, sensitive to only the uppermost crystal layer. As an example, diopside chain silicate crystals are highly oriented at the glass surface. Their SiO_2-chains, which are stretching along the c-axis, preferentially grow parallel to the glass surface ([001] ∥ S) [25,26]. Recently, this orientation was confirmed and proved to occur even for separate diopside crystals down to 700 nm in size [27].

Preferred crystal orientation also appears for fresnoite, a sorosilicate, where SiO_2 –TiO_2 layers often grow parallel and the c-axis is more or less perpendicular to the glass surface ([001] ⊥ S) [18,20,28,29]. The degree of crystal orientation, however, is less pronounced. In the case of Ba fresnoite glasses, other preferred crystal orientations have been reported. Surface crystals grown at temperatures between 790 °C and 970 °C on Ba fresnoite glasses with the molar composition 2 BaO–TiO_2–x SiO_2 (x = 0.75–3.0) showed an orientation of the crystallographic c-axis that was inclined at 60° to the glass surface normal [18,30,31]. This orientation of the c-axis can be accompanied by a parallel orientation of the (221) plane [31] or a perpendicular orientation of the crystallographic [101] direction with respect to the glass surface [18,30].

The only explanation for the differences in crystal orientations close to the surface layer is the process of oriented crystal nucleation [11,18]. The underlying mechanisms, however, are still under debate and none of the discussed hypotheses fully explain the observed crystal orientation data [23,27]. A possible reason may be the fact that EBSD studies were mainly performed on large surface crystals, which underwent crystal impingement. As crystal orientation can change during crystal growth [16,17], crystal–crystal interactions may have influenced the observed crystal orientation. An investigation of the crystal orientation on a surface with separated surface crystals has so far only been carried out for glass with the molar composition 8 BaO–8 SrO–34 ZnO–50 SiO_2 [32] and for diopside glass [27]. In addition, only surfaces crystallized in ambient air were investigated [18,30,31] in detail, while dendritic growth under vacuum conditions has been described in one publication [11].

Hence, it remains unknown whether a variation in the annealing atmosphere has an influence on the orientation of surface crystals and might control crystal orientation at the uppermost glass surface layer. In contrast to previous studies on BTS, the present investigation is conducted on freshly fractured surfaces, which are almost defect-free. Polishing alters the surface chemistry and causes non-randomly oriented surface defects, which produces oriented nucleation and affects crystal growth [18,33]. This study further focuses on the influence of the annealing atmosphere on the crystal morphology and orientation of Ba fresnoite crystals ($Ba_2TiSi_2O_8$, BTS) growing from the surface of a 2 BaO–TiO_2–2.75 SiO_2 glass.

2. Experimental Section

2.1. Samples

A glass of the composition 2 BaO–TiO_2–2.75 SiO_2 (34.8 BaO–17.4 TiO_2–47.8 SiO_2, mol %) was prepared from $BaCO_3$ (SABED), TiO_2 (VEB Jenapharm Laborchemie Apolda)

and SiO_2 (Carl Roth) raw materials. A 0.75 mol (about 8 mol %) excess of SiO_2 with respect to the BTS crystal composition ($Ba_2TiSi_2O_8$) was used to retard volume-induced nucleation. The batch was melted in a 250 mL Pt crucible at 1530 °C in an inductively heated furnace. After keeping at 1530 °C for 30 min, the melt was stirred for 1 h at 60 rpm. The melt was then poured onto a pre-heated steel mould (400 °C), held at 740 °C in a laboratory furnace for 1 h and then cooled to room temperature. Glass bars were cut from the glass block and fractured into pieces of 5 × 5 × 5 mm by using a running plier tool, which allowed for producing a freshly fractured low-defect surface flat enough for further analysis (e.g., EBSD).

Immediately after fracture, these pieces were heat-treated in a vacuum tubular furnace (F-VS 70-200/13, GERO Hochtemperaturöfen GmbH) in dry air (48 ± 5 ppmv water), argon (≤3 ppmv) and vacuum at 0.16 mbar (after flushing with N_2 ≤ 5 ppmv). Humidity was measured with a TF-2R-TOE-1 sensor (PANAMETRICS, Germany). Samples were heated at 24 K/min to 825 °C and held for different annealing times to ensure sufficiently large crystals. Annealing in ambient air (43% rh, 20 °C) was performed in a glass tube furnace (Linn High Therm GmbH, Eschenfelden, Germany, 1992).

2.2. Methods

Laser scanning microscopy (LSM) analyses were performed using a light microscope (Zeiss Axio Imager.Z1m) equipped with a confocal laser scanning module (series 700 including an argon laser 488 nm). Atomic force microscopy (AFM) investigations were performed in ambient air using a JPK NanoWizard4 with a soft cantilever operating in contact mode. For scanning electron microscopy (SEM) and electron backscatter diffraction (EBSD) analysis, all samples were coated with a carbon layer and contacted with Ag paste to avoid surface charging. While SEM analyses were performed by using a Jeol JSM-7001F, EBSD measurements were realized with an HITACHI SU-70 equipped with a Schottky emitter as well as an EDAX EBSD system containing an Hikari camera at the IMWS in Halle. EBSD scans were performed using an acceleration voltage of 20 kV and were captured and evaluated using the software OIM DC v5.31 and OIM Analysis v7.31. All scans were performed using a step width of 1 µm up to 250 nm. The recorded EBSD patterns were analyzed using a material file based on the ICSD dataset number 4451. Scanning transmission electron microscopy (STEM) was performed using an FEI Titan^3 G2 80-300 aberration corrected microscope. A lamella in cross-sectional geometry was extracted in situ and thinned to electron transparency using a Zeiss CrossBeam AURIGA.

X-ray diffraction (XRD) was performed using a Rigaku MiniFlex 300 with Cu Kα radiation and a θ–2θ arrangement in the 2θ range from 10 to 90° to identify crystalline phases. The recorded XRD patterns were interpreted by comparison with the ICDD database.

Thermal analysis was performed by differential scanning analysis (DTA, self-constructed) and dilatometry (DIL, 402 PC NETZSCH) using different powder grain sizes, bulk samples, different heating rates and several heating–cooling cycles. The glass transition temperature (T_g = 740 °C ± 5 °C) and the crystallization temperatures were determined by conventional tangent method. As an example, crystallization temperatures for a heating rate of 10 K/min and a grain size fraction of 56–63 µm were $T_{x,onset1}$ = 861 °C, $T_{x,max1}$ = 896 °C and $T_{x,offset1}$ = 916 °C for the first crystallization peak (fresnoite) and $T_{x,onset2}$ = 1131 °C, $T_{x,max2}$ = 1137 °C and $T_{x,offset2}$ = 1142 °C for the second crystallization peak (cristobalite). These values shifted with heating rates and powder size fractions.

3. Results

3.1. Crystal Morphology

Depending on the annealing atmosphere, different crystal morphologies developed on the fractured sample surfaces, and different annealing times were necessary to reach a similar crystal size (Figure 1).

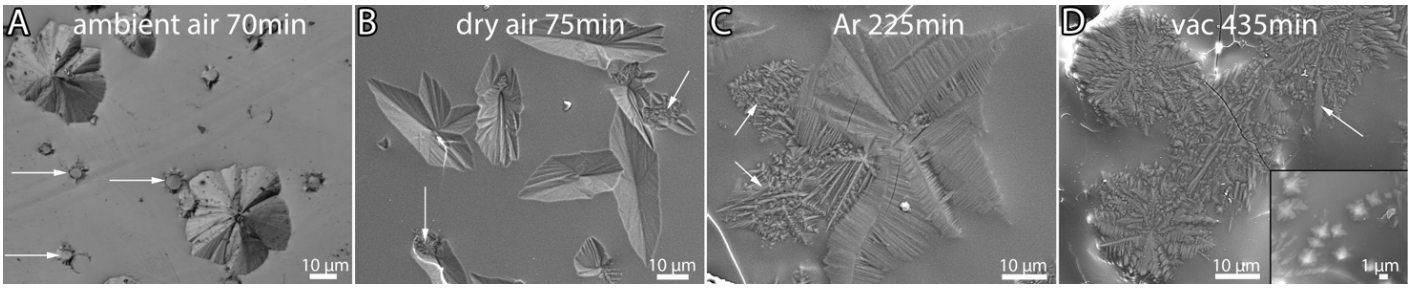

Figure 1. SEM images of freshly fractured glass surfaces heat-treated in different atmospheres. (**A**) Ambient air: compact crystal arrangements and small circular structures (arrows). (**B**) Dry air: spear-head-shaped compact crystals and small dendritic crystals (arrows). (**C**) Argon: platy aggregates of straight to curved central lines with ramifications accompanied by dendritic crystals (arrows). (**D**) Vacuum: radially arranged dendrites and few needle-like crystals (arrow). The zoom-in shows a second generation of small crystals (bimodal distribution).

3.1.1. Ambient and Dry Air

Fractured samples crystallized in ambient air exhibit compact-radial crystal arrangements of up to 40 µm in size (Figures 1A and 2A). Simultaneously, smaller circular structures of 5–10 µm in size appear. Samples heat-treated in dry air exhibit compact spear-head-shaped crystals with a foliaceous texture (Figures 1B and 2B). Sometimes, these crystals form star-like arranged aggregates (Figure 1B) as if crystal nucleation was triggered by the same nucleation site. In addition, small flocculent, partially dendritic crystals occasionally occur (Figure 1B, arrows), as well as circular structures similar to the ambient air samples, but larger in size (Figure 2B, arrows). As shown in Figure 2B, spear-head-shaped crystals appear as the dominant crystal morphology. Their foliaceous texture indicates dendritic crystal growth as expected for the given SiO_2 excess of the parent glass. Previous studies [31] on the same glass composition also reported dendritic growth of fresnoite into the glass volume. These studies, however, were focused on fully crystallized surfaces with enhanced surface roughness [18,30,31]. Therefore, to the best of our knowledge, the morphology of individual crystals on the surface has not been documented. Surprisingly, the spear-head-shaped morphology of the crystals formed in dry air in the present study is similar to the "compact, regularly shaped crystals" that developed during in situ experiments in vacuum at 830 °C, reported by Wisniewski et al. (2013) [30].

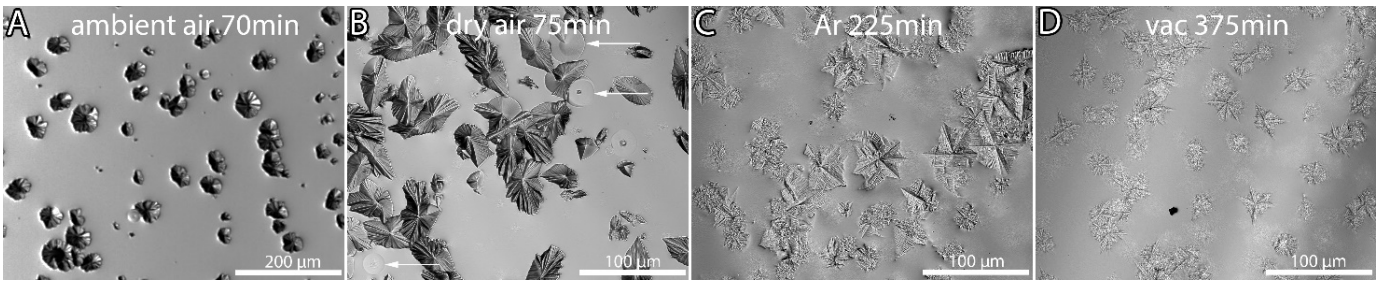

Figure 2. LSM overview images showing that the crystals in Figure 1 are representative.

In addition to the spear-head-shaped crystals, circular structures appeared on the glass surface after annealing in dry air (Figures 2B and 3A–C). Some of these circular structures appeared flat, showing lines radiating from a central point (Figure 3A). In some cases, these points might have served as a nucleation site for spear-head-shaped crystals (Figure 3B,C). Smooth circular structures (lacking the radial lines and less flat) occur more frequently. They sometimes develop radially arranged lines at their central points or at their rims, where the crystal growth of spear-head-shaped crystals develops (Figure 3B,C).

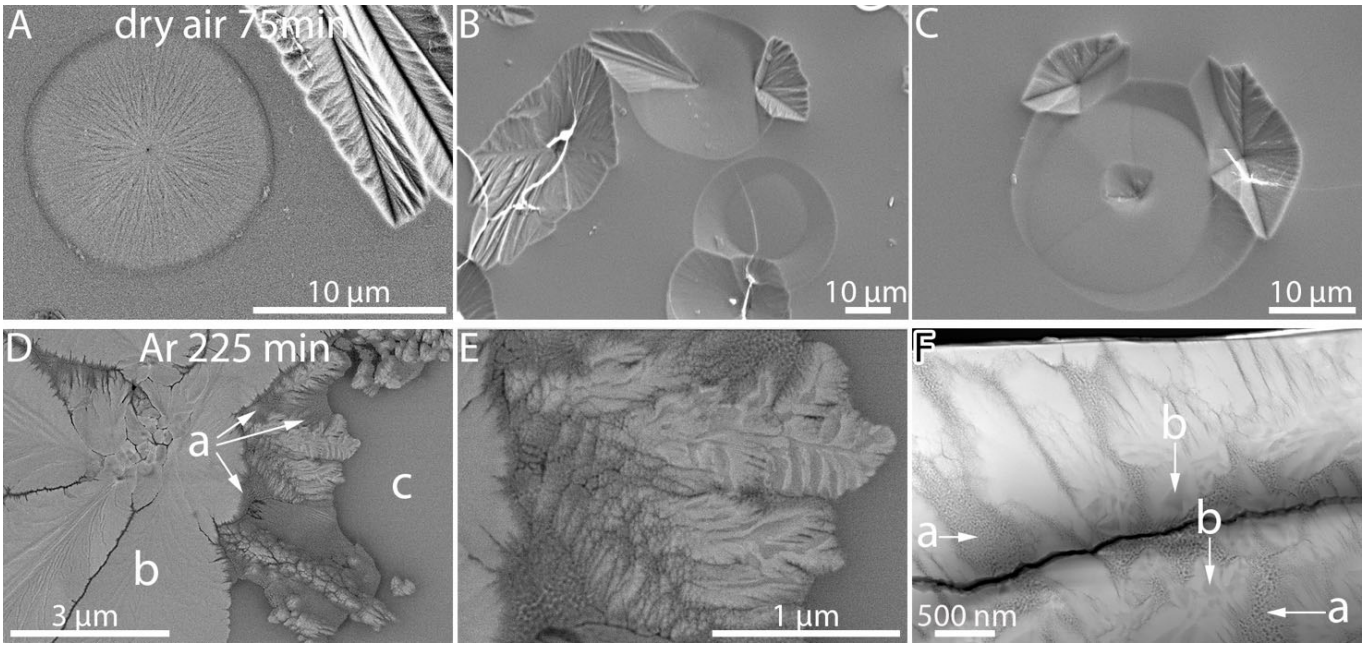

Figure 3. SEM details of samples crystallized in dry air (upper row) and in argon (lower row). (**A**) Low-angle BSE image of a flat circular crystal. Note the black dot in the center and the radially arranged lines. (**B**) Circular structures and spear-head-shaped crystals. Note the radial lines in the lower circular structure, the flat central plateau in its upper neighbor and the spear-head-shaped crystals within the uppermost sphere. (**C**) A circular structure with spear-head-shaped crystals growing from the center and the margins. (**D**) Dendritic crystals (b) are surrounded by glass (c). The crystal glass interface is indicated by different contrast (a). (**E**) Detail of region a showing the dotty structure of the area around the dendrites. (**F**) STEM micrograph. The lamella has been cut perpendicular to the sample surface, which is located at the top. Arrows (a) point to possible phase-separated SiO_2 droplets. Arrows (b) point to core texture of the sub-surface crystals.

3.1.2. Argon

On fractured surfaces in argon, crystal growth is slower and only small radially arranged dendritic crystals could be observed at 75 min annealing (not shown). These dendrites were mainly unbranched to weakly branched or showed parallel arranged ramifications. Mostly, these very thin ramifications grew vertically (90°), diverging from a main branch. To reach a similar crystal size, 225 min annealing was required, and crystals grew highly structured with lamellar-platy ramifications in a star-like arrangement accompanied by radially arranged dendritic areas (Figures 1C and 2C).

More detailed investigations (Figure 3D) indicate fine-grained structures (a) appearing darker compared to the dominating crystal phase (b) and the glass matrix (c). The structure of region (a) was studied by scanning transmission electron microscopy (STEM) (Figure 3F). It consists of small-grained areas (a), surrounded by brighter dendritic crystals. Furthermore, starting at about 500 nm depth from the surface, these crystals exhibit a darker shaded core (Figure 3F region b). No such core structures were found at the immediate surface, neither in the STEM sample nor in the SEM analysis nor in the AFM measurements.

3.1.3. Vacuum

For fractured samples annealed in vacuum, crystal growth is even slower than that developed in argon atmosphere. Only very small flocculent crystals of an irregular shape were observed at 75 min annealing time (not shown). From these flocculent crystals, radially arranged and strongly branched dendrites developed during 435 min/375 min of annealing (Figures 1D and 2D). Between these dendrites, a residual glassy matrix was observed. Needle-like crystals with slightly rough boundaries were found, which can

be attributed to dendritic arrangements (Figure 1D, arrow), either weakly branched or unbranched. Apart from the large crystals, some considerably smaller crystals were found at 435 min, showing star-like shapes, which indicate a second crystal generation (Figure 1D, detail) possibly caused by additional nucleation. In accordance with the literature [30], and intensively discussed within, a bimodal size distribution was only observed after a heat treatment in vacuum. Independently of the atmosphere, we have observed a broad range in crystal size, suggesting simultaneous crystal nucleation and growth as frequently reported in the literature [30,33,34].

3.2. Surface Topography

In dry air (Figure 4A), the crystallized fractured samples show pyramidal-shaped surface depressions up to 6 µm deep. The circular structures appear conically shaped and as deep as the crystalline ones, sometimes forming inner plateaus. The conical shape was predominantly observed for circular structures with a pronounced radial and concentric line pattern (Figures 4A, 5 and S3). In contrast, the textures are less pronounced on other circular structures (Figure 5E,G,H). These flatter circular structures were better distinguished from the surrounding glass by mapping the lateral force (friction) signal in atomic force microscopy (AFM) (Figure 5E,F). Tiny particles were often observed in the centers of the circular structures (Figure 5A,C,E–J), that are also visible in the low-angle BSE image (Figure 3A). Such possibly air-born particles or precipitates are known to promote crystallization [21], which, in turn, explains the development of the circular arrangement of crystals around them, shown as a radial line pattern. An LSM 3D image of a sample crystallized in ambient air is provided in the Supplementary Materials (Figure S4). It shows similar depressions of crystals and circular cones as the dry air samples.

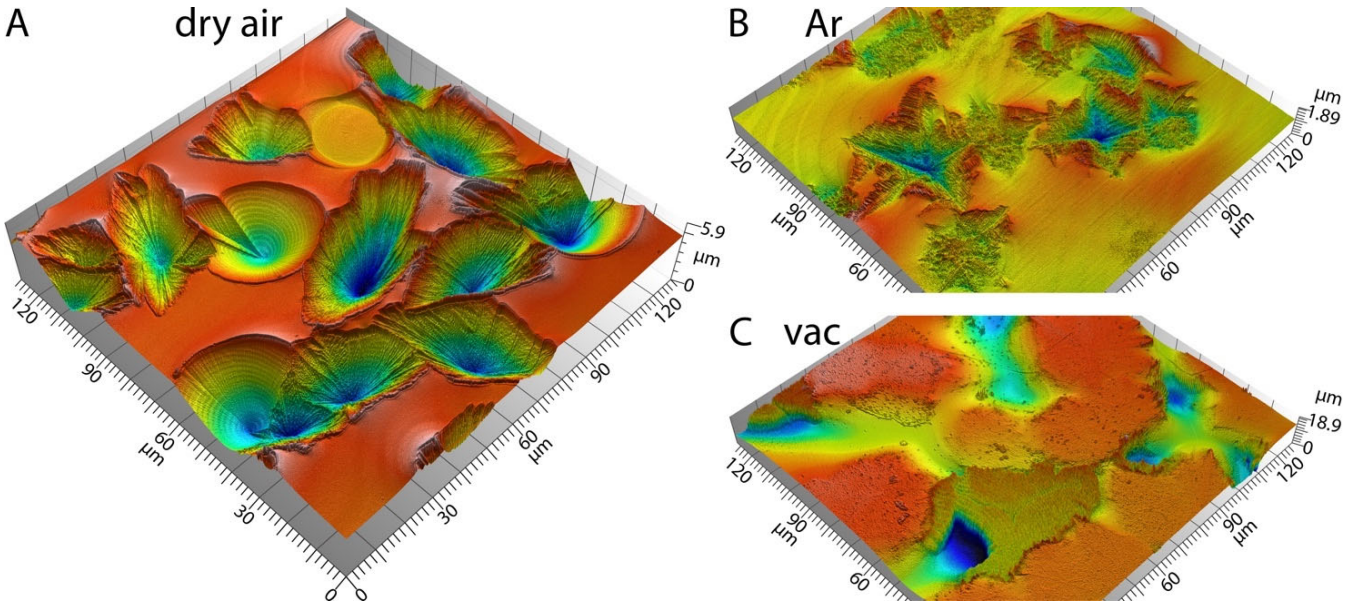

Figure 4. LSM 3D-images of crystallized surfaces in dry air (**A**), argon (**B**) and vacuum (**C**). The crystals and circular structures of the air and argon samples grow toward the bulk of the samples and form valleys. In vacuum, the crystals are the plateaus and the surrounding residual glassy matrix forms holes. Some branched crystals in argon atmosphere protrude from the surface.

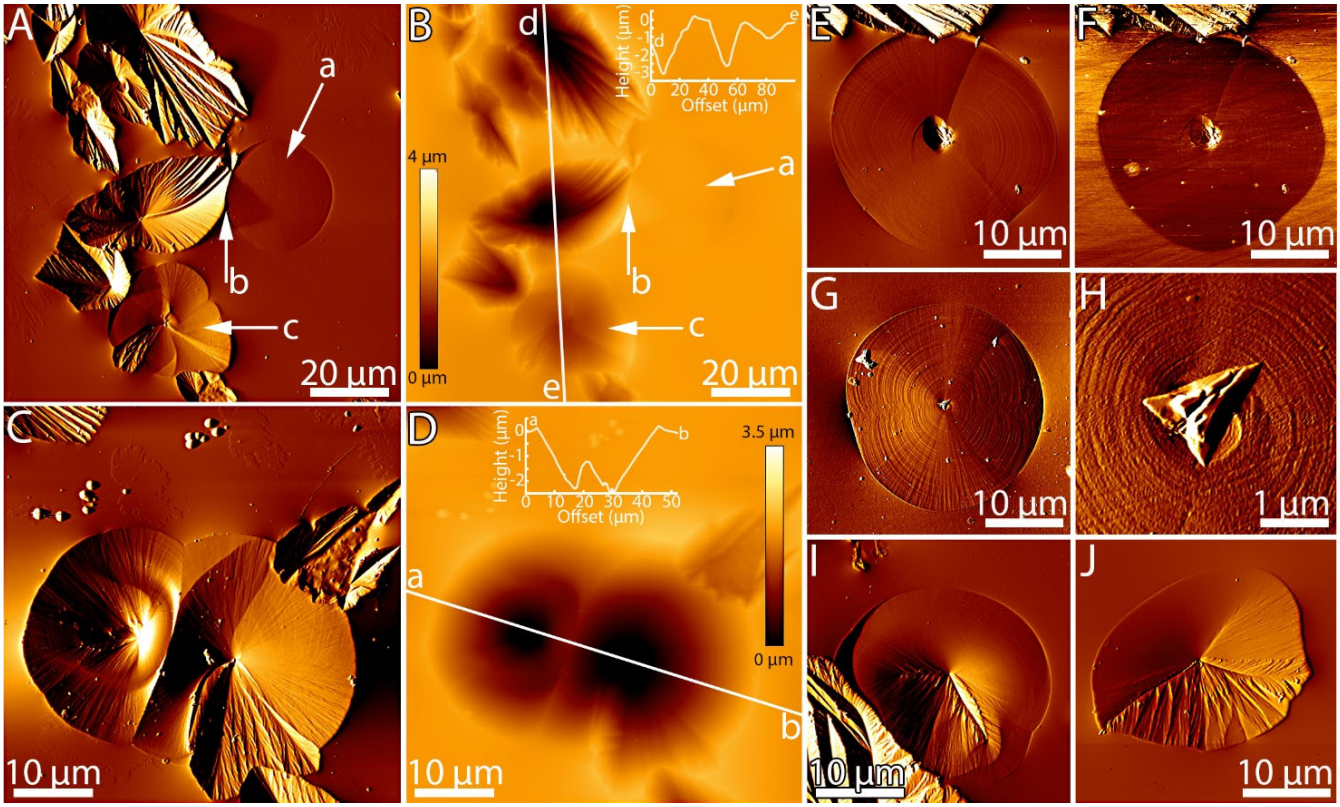

Figure 5. AFM images of samples annealed in dry air. AFM modes: (**B**,**D**) = topography; (**F**) = friction; (**A**,**C**,**E**,**G**–**J**) = vertical deflection signal. (**A**) + (**B**) Spear-head-shaped fresnoite crystals grow toward the sample bulk. Circular structures can be flat (a) or form a cone (c). The circular structures affect the growth of fresnoite crystals and cause bending (b). The profile line (d,e) illustrates the surface topography. (**C**) + (**D**) Fresnoite crystals grow favored at the centers or phase boundaries of cone-shaped circular structures with radial lines. Note the height differences in the profile line (a,b). (**F**) Friction mode confirms that the circular shapes are chemically or structurally different from the matrix. (**E**) + (**G**) Circular structures with radial and concentric lines. (**H**) Detail of G. A fresnoite crystal is growing in the center. (**I**) + (**J**) Advanced transition from a circular structure to fresnoite crystals.

In argon atmosphere (Figure 4B), the centers of the crystal aggregates also appear pulled into the sample surface. This effect, however, is less pronounced (<2 µm) than that in dry (<6 µm) and ambient air (Figure S4). However, similar depressions of crystals and circular cones were found both in ambient air and in dry air. With increasing distance from the center, some crystals protrude from the surface.

Under vacuum (Figure 4C), radially arranged flat dendrites are leveled at the outermost sample surface, whereas deep pockets occur between them (Figure S5).

3.3. Crystal Orientation

Although different crystal sizes and morphologies occur in different annealing atmospheres, only fresnoite was detected by XRD analysis (Figure S1, Supplementary Materials). The diffraction patterns observed for different annealing atmospheres, however, indicate different non-random crystal orientations, which seems least pronounced for annealing in vacuum.

Crystal orientation was therefore studied with EBSD. The inverse pole figure maps show which crystallographic axes are aligned with the sample surface normal. For quantitative analysis, orientation histograms for the a- and c-axis (<100> and [001]) as a function of the angular distance to sample normal are given in the Supplementary Materials (Figure S6). Pole figures give insight into how any given, fixed crystallographic axis is oriented with

respect to the sample surface. The color scale indicates by which factor the maximum of the orientation distribution function surpasses random distribution.

3.3.1. Ambient and Dry Air

Figure 6 refers to a sample annealed in ambient air. In this case, where circular structures occur more frequently, the c-axis [001] is often oriented perpendicular to the surface plane or 45° inclined from the sample surface normal (bottom pole figure). Most strikingly, the texture intensity (i.e., the degree of non-random orientation) is larger than that in dry air (see below).

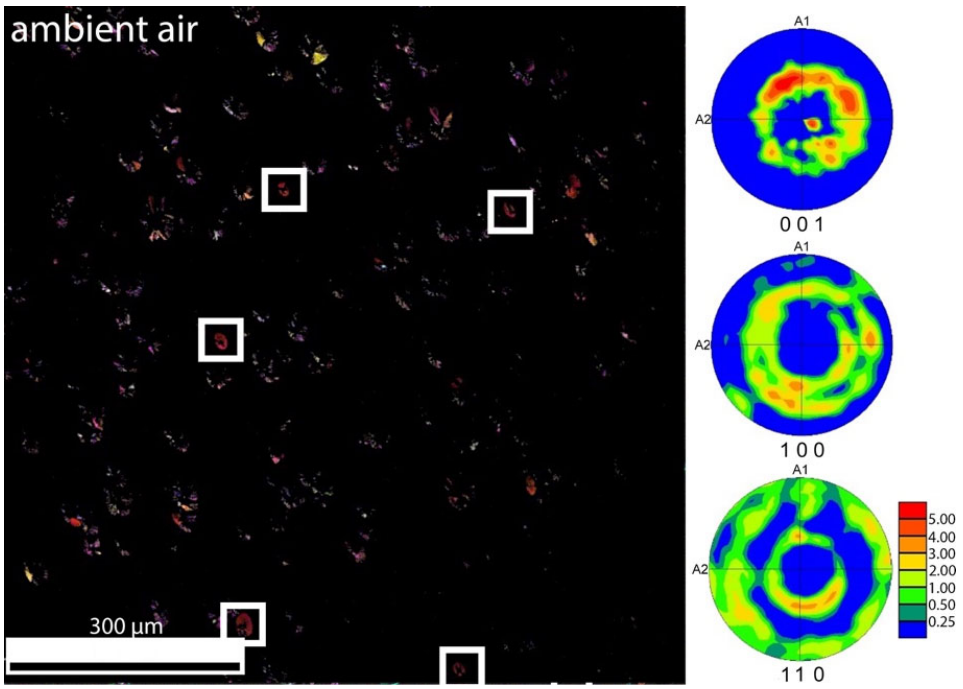

Figure 6. Texture and orientation data for a sample heat-treated in ambient air. Left: 001 inverse pole figure mapping. Right circles: pole figures 100, 001 and 110. The boxed red dots are frequently occurring circular structures.

Figure 7 (right, upper pole figure) shows that the c-axis of fresnoite surface crystals grown in dry air preferentially lies within the surface plane or, much less pronounced, 60° tilted from the surface normal. The a-axis distribution exhibits orientation distribution maxima tilted approximately 15°, 41° and 72° from the surface normal. The [001] inverse pole figure (top right in the inverse pole figure map) reveals that there is a maximum in the z-axis orientation distribution close to the [310] direction, perpendicular to the surface. While a large fraction of crystals in the dataset are spear-head-shaped, there are two peculiar crystals in the [001] inverse pole figure that have a close to circular form and are oriented with the c-axis being perpendicular to the surface (white boxes).

3.3.2. Argon

The surface crystals formed under argon atmosphere (Figure 8) show a very broad distribution with a low degree of preferential orientations (225 min annealing time). The pole figures show that the c-axis is preferentially parallel to the sample surface. The histogram of the a-axis (Figure S6) shows peaks around 30° and 65° inclined from the sample normal.

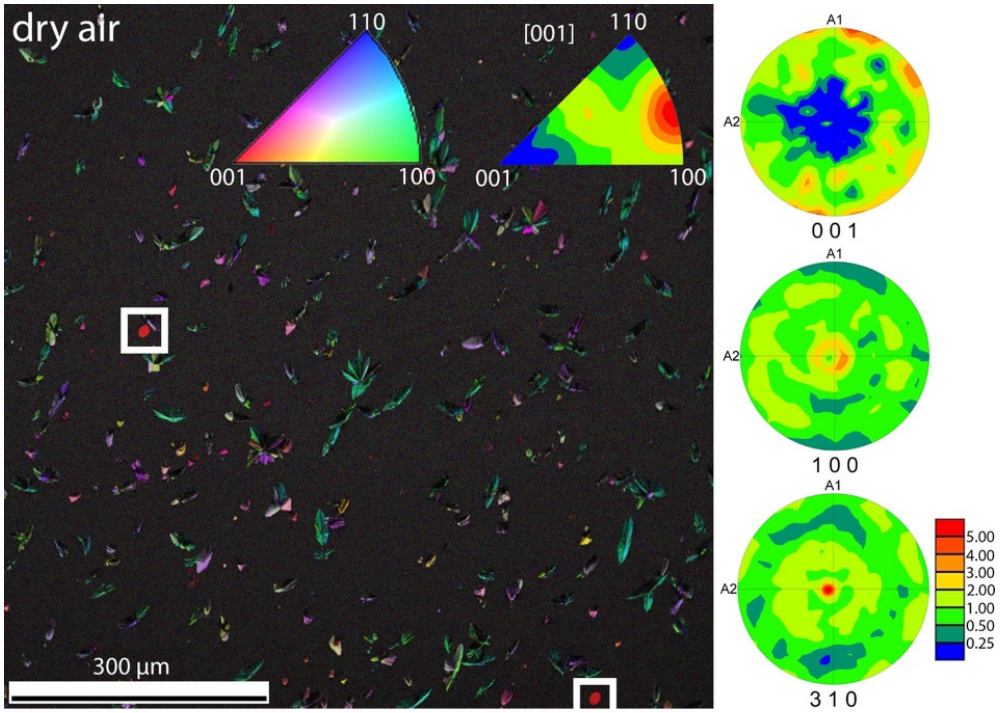

Figure 7. Texture and orientation data for a sample heat-treated in dry air. Left: 001 inverse pole figure mapping and [001] inverse pole figure of the texture (top right). Right circles: pole figures 001, 100 and 310. The boxed red dots are flat circular structures with a radial line pattern.

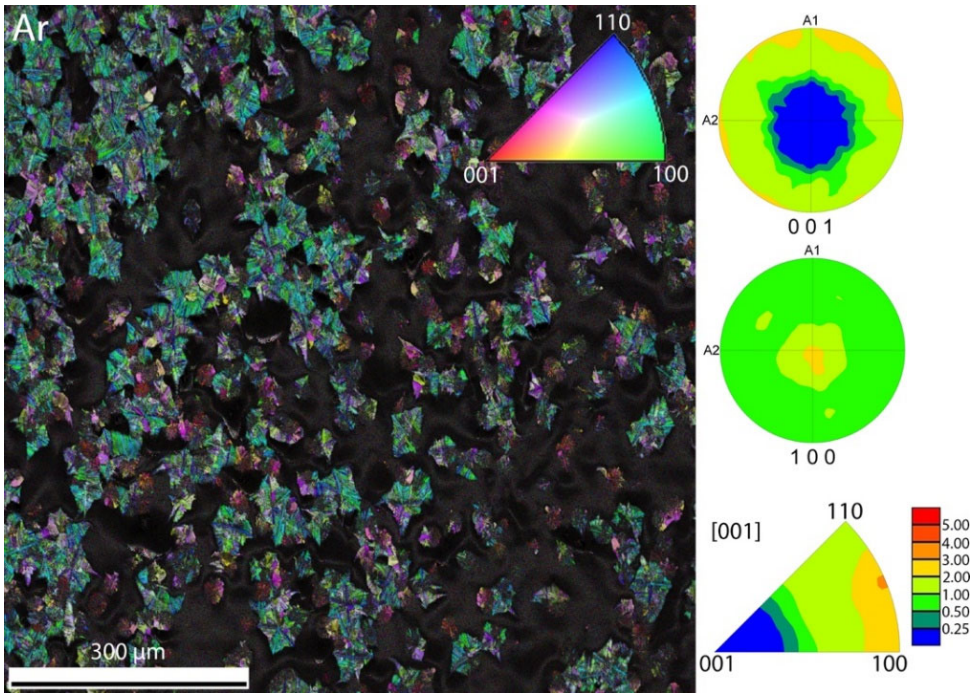

Figure 8. Texture and orientation data of a sample heat-treated in argon for 225 min. Left: 001 inverse pole figure mapping. Right circles: 001 and 100 pole figures, Bottom right: [001] inverse pole figure.

Figure 9 shows a sample annealed in argon for 75 min. Similar to Figure 8, the c-axis tends to be oriented rather than parallel to the sample surface, but less pronounced. This finding indicates that crystal orientation may change during growth or the related gradual manifestation of the surface topography shown in Figure 4.

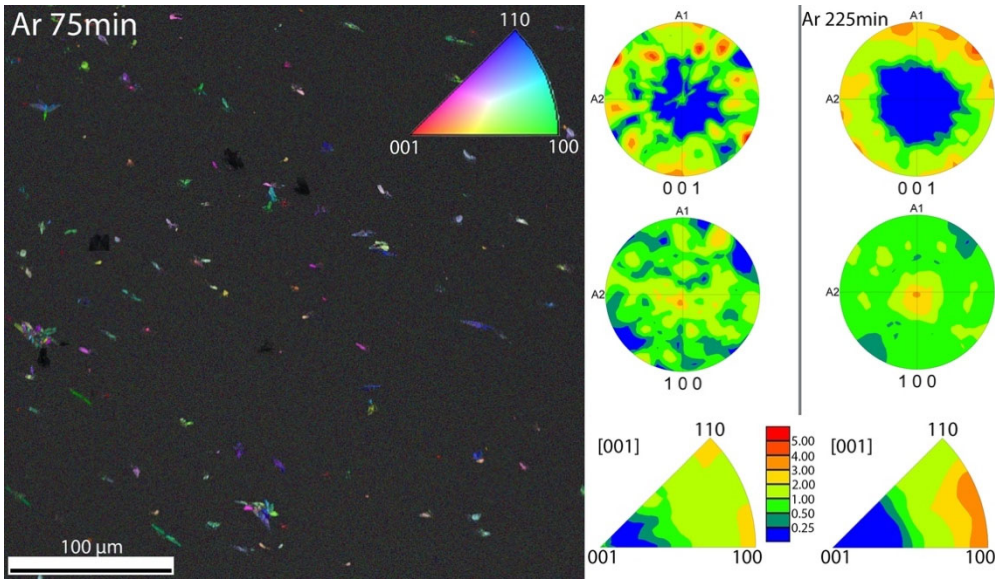

Figure 9. Texture and orientation data for a sample heat-treated in argon. Left: 001 inverse pole figure mapping, 100 and 001 pole figures and [001] inverse pole figure of the texture. Right column: Comparison with texture data obtained from a sample heat-treated for 225 min in argon atmosphere, obtained by cropping a similar-sized region of interest from the dataset shown in Figure 8.

3.3.3. Vacuum

The orientations of the crystals annealed in vacuum are very similar to those of the crystals formed in argon atmosphere (Figure 10). In particular, the a-axis histogram has peaks at the same positions (30° and 60°), albeit being comparably noisier (Figure S6). The c-axis histogram has only one very broad peak ranging from approximately 40° to 90° from the surface normal (Figure S6). In general, the sample contains more regions with small, strongly branched dendritic crystals and the fraction of successfully indexed data points is lower in this dataset and just includes the needle-like parts of the crystal arrangements.

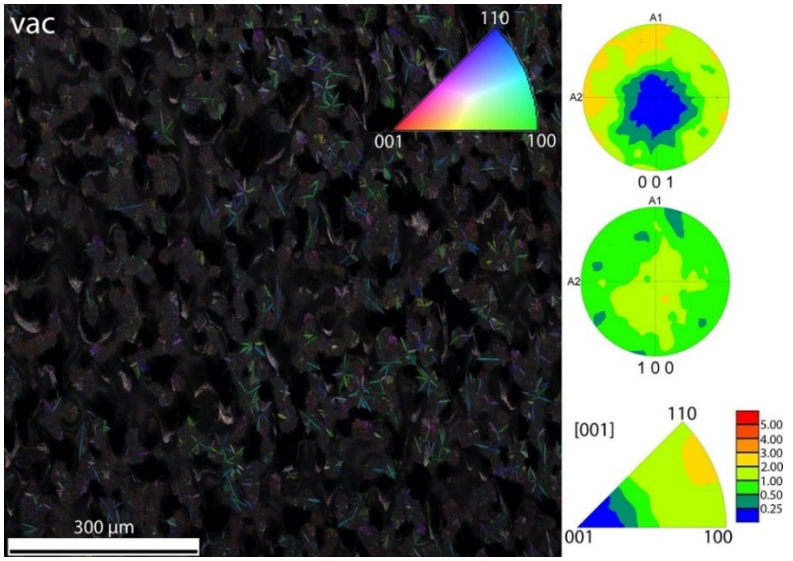

Figure 10. Texture and orientation data of a sample heat-treated in vacuum; 100 and 001 pole figures and [001] inverse pole figure of the texture; 001 inverse pole figure mapping.

3.3.4. Comparison, Details and Cropped Datasets

In all measurements, there were strong differences in data quality for the different morphologies of the crystals. Generally, the larger crystals exhibited high-quality patterns

and could be clearly identified as fresnoite using a material file based on ICSD entry no. 4451 [35,36]. The small, strongly branched dendrites provided significantly weaker Kikuchi patterns, which is reflected in the image quality parameter being lower in these regions. This is likely caused by the inclusion of a residual glassy matrix between dendrite branches, which reduces the homogeneity of the crystal structure within the interaction volume contributing to the Kikuchi pattern.

To obtain more insight into the microstructure of individual crystals and possible growth mechanisms involved, EBSD scans at an increased resolution have been performed for samples heat-treated in argon atmosphere and vacuum, since those possess a high fraction of crystals with dendritic morphology.

In Figure 11, image quality and inverse pole figure mappings are shown for the sample heat-treated in argon for 225 min. Additionally, an analysis of the axis around which neighboring grains are rotated with respect to each other has been performed and the grain boundary has been colored accordingly, using the same color coding as the inverse pole figure. Even at increased magnification, the dendritic crystals exhibit lower quality diffraction patterns and a higher degree of granularity. The plate-like structures often show rotations around the c-axis between grains. As can be seen in the misorientation profile D, typical misorientation angles at the grain boundaries are between 10° and 15°. Together with the lamellar structure, this could indicate twinning of the crystals. The dendritic regions are not homogeneously oriented, but exhibit a large degree of misorientation from the center outward, as can be seen in misorientation profile E. The point-to-origin misorientation changes almost continuously, with jumps in the order of 5° occurring between the segments of the cluster. Interestingly, crystal clusters oriented with the c-axis perpendicular to the surface occur in the dendritic regions, which have generally not been observed for the plate-like structures' grown areas.

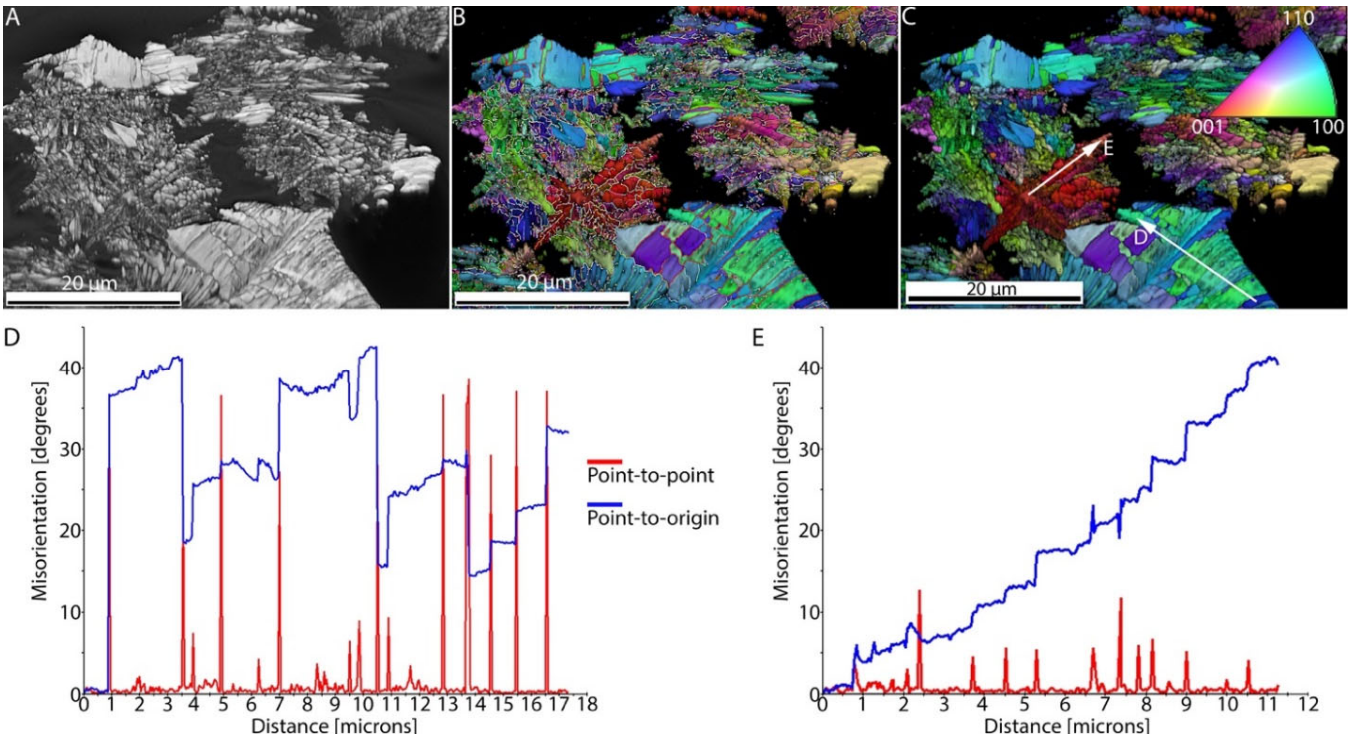

Figure 11. High-resolution EBSD data of a sample heat-treated in argon. (**A**) Image quality. (**B**) Grain boundaries are color-coded to show the axis of relative rotation between neighboring grains, using the same color coding as the IPF. (**C**) 001 inverse pole figure mapping with traces of the misorientation profiles. (**D**) + (**E**) Misorientation profiles along arrows (**D**,**E**) in Figure 11C.

High-resolution EBSD data for the sample heat-treated in vacuum are shown in Figure 12. Compared to the high-resolution data for the sample heat-treated in argon, the data quality in the dendritic regions is even lower, in agreement with the image quality map. The clusters of dendrites also seem to be even more fragmented. The degree of crystallinity in these regions is lower and, correspondingly, the amount of residual glassy matrix is higher. However, another cause of the lower data quality might be the high degree of surface deformation that this sample exhibits, which makes proper signal processing more complicated. No similar twinning around [001], as for the crystals formed in argon, was observed. The elongated, needle-like crystals frequently occurring in this dataset generally showed a very high degree of orientation homogeneity (Figure 12B, arrow). The misorientation profile shows that the point-to-origin misorientation is less than 5° over about 10 µm. Due to the low data quality, misorientation analysis has not been reliably possible in the dendritic regions.

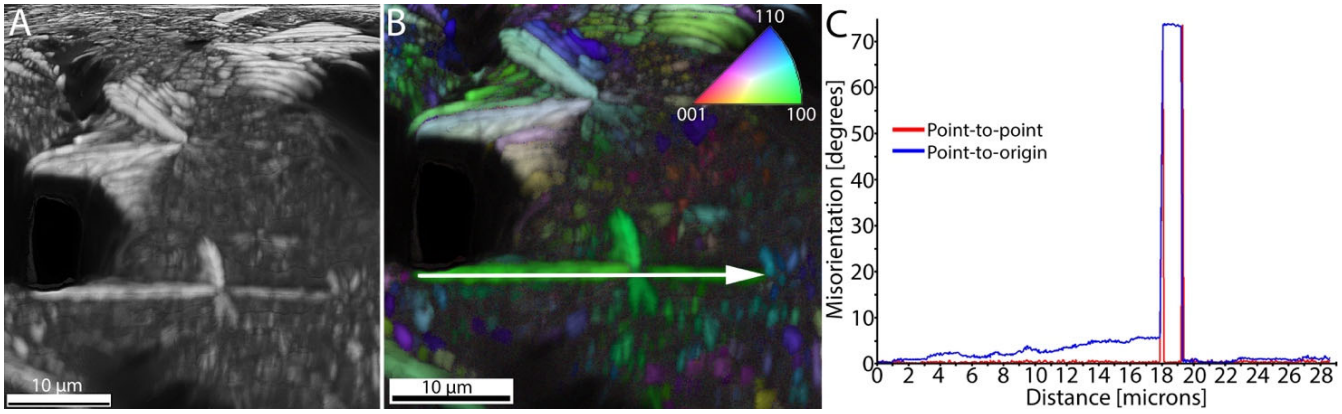

Figure 12. High-resolution EBSD data of a sample heat-treated in vacuum. (**A**) Image quality. (**B**) 001 inverse pole figure mapping with indicated profile line. (**C**) Misorientation profile along the profile line.

4. Discussion

Although only fresnoite could be detected by XRD analysis (Figure S1) for all different annealing atmospheres investigated here, our results clearly exhibit strong variations in crystal size and morphology, surface topography and crystal orientation.

4.1. Crystal Morphology

Different annealing times were required to reach a similar range of crystal sizes on fractured surfaces (70/75, 225 and 435 min for ambient/dry air, argon and vacuum, respectively), resulting in a non-quantitative crystal growth rate of 0.32 µm/min for argon and 0.1 µm/min for vacuum. Determining the growth rates for the air samples was not possible, because the experimental setup did not allow for the use of shorter annealing times than the ones chosen. The crystal growth rate was scaling with humidity. For ambient air 43% rh and for dry air, a 48 ppmv water content was measured, whereas the nominal humidity of the bottled argon was ≤3 ppm and that of vacuum can be considered even less (0.16 mbar of N_2 with ≤5 ppmv water at 1 bar). Interactions between water (from atmospheric humidity) and the glass surface can lead to the formation of silanol groups that enable the absorption of water by the glass [37]. As a result, the surface energy and viscosity of the glass-forming melt can substantially decrease [38], which increases the crystal growth rate. Vice versa, annealing in a dry atmosphere or in vacuum could even cause the near-surface depletion of the water dissolved during glass melting (e.g., 300 ppmwt in commercial soda lime silicate glass [39]). This effect may lead to a near-surface layer of increased viscosity.

The annealing atmosphere strongly affects the crystal morphology as well. With decreasing humidity, the dominant morphology appears more distorted, indicating a more

constrained crystal growth. Such a constraint seems reasonable as the BTS crystals must grow into a melt of a significant SiO_2 excess. Therefore, a progressively increasing SiO_2 enrichment and increased viscosity is expected to occur in front of the growing crystals. The presence of water can strongly decrease viscosity and could therefore reduce this effect.

On this basis, it is not surprising that the most compact and least distorted spherical surface crystals grew in ambient air, simultaneously with spear-head-shaped crystals. Figures 1–5, Figures S2 and S4 (Supplementary Materials) reveal different shapes and textures of these spherical structures, ranging from smooth to foliaceous textures and from spherical to rounded polyhedra. Their size is often similar to that of the spear-head-shaped crystals, and they often cluster as rosettes. These observations suggest that the spherical structures might be caused by the same crystals, but less distorted and differently oriented. Vice versa, the most distorted crystal morphology, i.e., finely branched dendrites (Figure 1D) with only a few more compact needles, seems to occur in vacuum. Radially arranged dendrites were observed by Wisniewski et al. (2013) [30] during in situ crystallization at 790 °C in an electron microscope for a glass with the same composition presented here. During their crystallization experiments in vacuum at 830 °C, additional compact spear-head-shaped crystals were formed. The absence of spear-head-shaped crystals at 790 °C in the present study under vacuum can be attributed to the different experimental conditions. While in the present study, rectangular glass pieces with freshly fractured surfaces were crystallized in vacuum (0.16 mbar), the in situ experiments by Wisniewski et al. (2013) [21] were performed in a high vacuum atmosphere on polished samples. Furthermore, we used different heating rates, i.e., 24 K/min vs. 10 K/min used by Wisniewski et al. (2013) [21]. Since several experimental parameters were varied compared to Wisniewski et al. (2013) [21], interpretation with regard to the causes of different crystal morphologies is rather speculative.

Dendritic crystal morphology also occurs for annealing in argon atmosphere. In contrast to vacuum annealing, however, more compact unbranched to weakly branched spherulites showing parallel arranged ramifications have been observed. It should be noted that, apart from differential scanning calorimetry (DSC) measurements to calculate the activation energy of crystallization as well as the Avrami index of fresnoite [34], no reports on the crystallization of fresnoite glasses under argon atmosphere were presented in the previous literature. Moreover, to the best of our knowledge, there are no studies revealing the morphology of surface fresnoite crystals formed in glasses under argon atmosphere.

4.2. Surface Topography

Figures 4, 5 and S4 reveal that the central points of crystal aggregates are often pulled below the surface level, whereas the crystal aggregate margins seem to stick to the melt surface. This "pulling" effect is most pronounced for air, where the central points of spear-head-shaped crystal aggregates and conical circular crystals can reach 4–6 µm in depth. A similar but weaker effect is seen for argon (<2 µm depth). The ratio between this depth and the size of crystal aggregates is comparable in both cases. In vacuum, the crystals were highly distorted and grew more slowly without any pulling effect. In this sense, the pulling effect seems to scale with humidity, crystal size and distortion-free crystal growth.

The density of the glass (4.07 ± 0.01) g/cm^3 differs from the density of the fresnoite crystals (4.43 ± 0.02) g/cm^3 by about 8 % to 9 % [40]. This is interesting in terms of compaction but negligible compared to the surface tension effect which can be considered a possible explanation for the observed "pulling" effect. These phenomena are known to control the microstructure evolution during sintering of glass powders or glass matrix composites and to be effective even for viscous melts [41]. As interfacial energies for different crystal faces can differ, this effect may also cause oriented nucleation [23,27] or a "pulling in" or "pushing out" of differently oriented crystals, as observed by Diaz-Mora et al. (2000) [40]. If a certain angle < 180° between different spear-head-shaped crystal segments is preferred, crystal clusters cannot grow entirely flat. Instead, they tend to form radially kinked surface depressions. Such a typical angle is seen at the outer edge of the

pyramidally shaped valleys in Figures 1 and 3, as well as within the single spear-head-shaped crystal growing within a spherical cluster in Figure 4A. As the growing crystal cluster remains wet during growth to minimize its surface energy balance and to ensure its further growth into the melt, its radial growth will pull it into the melt.

The surface topography of the fractured sample annealed in vacuum (Figures 4C and S5) cannot be explained this way. The observed topography rather reminds of melt pockets caused by a volume shrink of the melt or by the overall expansion of the crystalline surface layer during growth. Strong deviations between the melt and crystal aggregates and related stress accumulation during cooling are indicated by a cracked surface (Figure S5).

4.3. Crystal Orientation

Figures 6–10 show that the degree of non-random crystal orientation decreases from annealing in ambient air, via dry air and argon to annealing in vacuum. Since these atmospheres strongly vary in humidity (10^4, 48, $\leq$3 and $\leq 5 \times 10^{-3}$ ppmv), the degree of preferred crystal orientation could, thus, be related to humidity or its effect on crystal growth (Figures 1 and 2). In this sense, the crystal growth rate, the tendency for less distorted crystal growth, the manifestation of the pulling effect and the degree of non-random crystal orientation all scale with humidity.

All these effects seem reasonable as the fresnoite crystals grow in a melt with about 8 mol% excess of SiO_2. The resulting increasing concentration of SiO_2 in front of the growing crystal would result in increasing stress constraints. Stress relaxation has been proposed to affect the texture at the immediate surface, which could explain the twinning of the large crystals and continuous misorientation within the dendritic regions observed for crystals formed under argon atmosphere (Figure 11). The presence of water decreases viscosity and could reduce this effect.

This observation suggests that non-random crystal orientation requires not only pronounced nucleation of oriented crystals, but also that the preferred orientation is not becoming lost during crystal growth. Such a change in crystal orientation is well known to occur when a different crystal orientation is preferred during nucleation (first, outermost layer) and further growth based on growth selection criteria (second layer) [23]. Other examples of stress-induced crystal orientation changes have been reported for laser patterning studies [42].

Consistently, Figures 8 and 9 show that crystal orientation changes during growth. The trend that the c-axis is preferably aligned to the sample surface as seen in Figures 7–10 obviously becomes more pronounced after prolonged growth. Vice versa, this finding may even hint at a very different crystal orientation during nucleation. Assuming that the least constrained crystal growth may best preserve the initial crystal orientation, Figures 6–9 indicate that the initial c-axis orientation could even be perpendicular to the sample surface. Such orientation is at least partially shown for annealing in ambient air (Figure 6), where the largest degree of non-random crystal orientation is seen.

This orientation has in fact been reported as a preferential c-axis orientation for STS (2 SrO–TiO_2–2.45 SiO_2) and BTG (2 BaO–TiO_2–2.75 GeO_2) fresnoite crystals [28,29]. Such initial crystal orientation during nucleation is easily explained by the different interfacial energies parallel and perpendicular to the cation modifier layers characteristic of the fresnoite structure, which are staggered along the c-axis [27,43]. Such a modifier layer would exhibit lower interfacial energy, and crystals oriented with [001] perpendicular to the surface would have all their higher-energy surfaces wetted by the melt. This particular orientation would preferably reduce the total energy of the system.

The preferred crystal orientation observed in Figure 6, however, does not fully agree with this picture at first glance. On the other hand, the present study demonstrates that surface crystal orientation can be affected by surface topography. Figure 4 shows that most of the crystal surfaces of the observed crystal aggregates are tilted away from the sample surface to a significant and typical amount. Crystal clusters forming depressions with characteristic non-randomly tilted depression flanks can, thus, systematically affect the

crystal orientation measured with EBSD. This effect may explain the observed preferred [310] orientation perpendicular to the surface (Figure 7, bottom pole figure) or the preferred 45–65° inclination of the c-axis from the surface normal (Figure 6, 001 pole figure).

In a similar sense, random surface roughening was found to cause a strong scatter in crystal orientation [27]. Due to the systematic nature of the surface texturing during the crystal growth shown here, dominating crystal orientation can even appear systematically changed by the angle at which the crystals growing is tilted due to the occurring pulling in phenomenon.

5. Conclusions

Surface crystallization of barium fresnoite glasses of the molar composition 2 BaO–TiO_2–2.75 SiO_2 at 825 °C in ambient/dry air, argon or vacuum led to the formation of barium fresnoite crystals with a different size, morphology and orientation. These changes correlated with changes in the humidity of the annealing atmosphere. The fresnoite crystals formed in a melt with about 8 mol% excess of SiO_2, resulting in an increase in SiO_2 concentration in the glassy matrix during crystallization. As a result, an increase in viscosity of the glassy matrix can be expected to occur during crystallization, and the presence of water can directly affect this viscosity and, thus, the crystallization behavior. As a result, the morphologically least textured surface crystals appeared when annealing in air, i.e., the atmosphere with the highest humidity, whereas in vacuum, i.e., the atmosphere with the lowest humidity, dendritic crystals appeared.

Crystal clusters were pulled into the glass melt during ongoing growth, creating surface topography characterized by up to 6 µm deep depressions. This effect scaled with the crystal size, morphology and humidity as well. The shape and size of these depressions forced the crystals to grow in a characteristic angle relative to the sample surface. Such a driving force for surface crystal orientation, to our knowledge, has so far not been described in the literature. The enhanced crystal orientation observed in EBSD analyses may be a result of several of those parameters, i.e., viscosity decrease, close to ideal morphology and systematic orientation changes due to evolved surface topography.

Non-random crystal orientation can be obscured by orientation changes occurring during crystal growth. This effect is expected to be particularly strong when the crystal stoichiometry differs from that of the parent melt, leading to the formation of a high viscosity residual glassy matrix. Vice versa, it is less pronounced in a humid environment, which decreases melt viscosity and changes the interfacial energy. This finding may explain why only the least textured circular crystals, observed during annealing in air, showed an orientation of their c-axis perpendicular to the sample surface.

Supplementary Materials: The following supporting information can be downloaded at: https://www.mdpi.com/article/10.3390/cryst13030475/s1, Figure S1: XRD-pattern of annealed 2BaO–TiO_2–2.75 SiO_2 samples; Figure S2: LSM image of a fully crystallized (fractured) sample surface heat-treated for 70 min in ambient air; Figure S3: Overview LSM image of freshly fractured glass surfaces 75 min annealed in dry air; Figure S4: LSM 3D image of a fractured sample 70 min annealed in ambient air; Figure S5: Overview SEM images of freshly fractured glass surfaces 435 min annealed in vacuum; Figure S6: EBSD histograms of the samples.

Author Contributions: This work is based on the Master's Thesis of M.F., who conducted most of the experiments under supervision of F.S., D.S.B. and R.M.; R.B. performed the EBSD analysis; S.C. performed the AFM analysis under supervision of E.G.; C.T. provided the data for the wet air samples; F.S. coordi-nated this work, produced the figures and wrote the main part of this manuscript. All the authors contributed to the internal review process and have read and agreed to the published version of the manuscript. All authors have read and agreed to the published version of the manuscript.

Funding: This work is part of the joint German Research Foundation (DFG) project RE 4146/1-1 and PA 3097/1-1 for which financial support by DFG is gratefully acknowledged.

Data Availability Statement: Not applicable.

Acknowledgments: Sample preparation and annealing studies were performed during a 5-month stay of M. Fleck at BAM. The authors express their gratitude to C. Blaeß and C. Meyer for experimental help and advice. S.C. thanks the Technical University of Ambato (UTA), its DIDE Department and F. Del Pozo for their help. A. Kemptner and C. Patzig are kindly thanked for FIB sample preparation and TEM analysis. We would like to thank five anonymous reviewers for the thorough evaluation of this manuscript and all the comments that helped to improve the quality of the paper. We acknowledge support by the German Research Foundation Projekt-Nr. 512648189 and the Open Access Publication Fund of the Thüringer Universitäts- und Landesbibliothek Jena.

Conflicts of Interest: The authors declare no conflict of interest.

References

1. Halliyal, A.; Bhalla, A.S.; Newnham, R.E.; Cross, L.E. $Ba_2TiGe_2O_8$ and $Ba_2TiSi_2O_8$ pyroelectric glass-ceramics. *J. Mater. Sci.* **1981**, *16*, 1023–1028. [CrossRef]
2. Halliyal, A.; Bhalla, A.S.; Markgraf, S.A.; Cross, L.E.; Newnham, R.E. Unusual pyroelectric and piezoelectric properties of fresnoite ($Ba_2TiSi_2O_8$) single crystal and polar glass-ceramics. *Ferroelectrics* **1985**, *62*, 27–38. [CrossRef]
3. Markgraf, S.A.; Halliyal, A.; Bhalla, A.S.; Newnham, R.E.; Prewitt, C.T. X-ray structure refinement and pyroelectric investigation of fresnoite, $Ba_2TiSi_2O_8$. *Ferroelectrics* **1985**, *62*, 17–26. [CrossRef]
4. Ting, R.Y.; Halliyal, A.; Bhalla, A.S. Polar glass ceramics for sonar transducers. *Appl. Phys. Lett.* **1984**, *44*, 852–854. [CrossRef]
5. Nagel, M.S. Phasen- und Texturanalyse Gerichteter, Durch Elektrochemisch Induzierte Keimbildung Hergestellter Fresnoit-Glaskeramiken. Ph.D. Thesis, Friedrich-Schiller-Universität, Jena, Germany, 2011.
6. Toyohara, N.; Benino, Y.; Fujiwara, T.; Komatsu, T. Enhancement of second harmonic intensity in thermally poled ferroelectric nanocrystallized glasses in the BaO-TiO_2-SiO_2 system. *Solid State Commun.* **2006**, *140*, 299–303. [CrossRef]
7. Masai, H.; Tsuji, S.; Fujiwara, T.; Benino, Y.; Komatsu, T. Structure and non-linear optical properties of BaO-TiO_2-SiO_2 glass containing $Ba_2TiSi_2O_8$ crystal. *J. Non-Cryst. Solids* **2007**, *353*, 2258–2262. [CrossRef]
8. Takahashi, Y.; Benino, Y.; Fujiwara, T.; Komatsu, T. Large second-order optical nonlinearities of fresnoite-type crystals in transparent surface-crystallized glasses. *J. Appl. Phys.* **2004**, *95*, 3503–3508. [CrossRef]
9. Kimura, M.; Fujino, Y.; Kawamura, T. New piezoelectric crystal: Synthetic fresnoite ($Ba_2Si_2TiO_8$). *Appl. Phys. Lett.* **1976**, *29*, 227–228. [CrossRef]
10. Osman, R.A.M.; Idris, M.S. Electrical properties of fresnoite $Ba_2TiSi_2O_8$ using impedance spectroscopy. *Adv. Mater. Res.* **2013**, *795*, 640–643. [CrossRef]
11. Wisniewski, W.; Thieme, K.; Rüssel, C. Fresnoite glass-ceramics—A review. *Prog. Mater. Sci.* **2018**, *98*, 68–107. [CrossRef]
12. Keding, R. Elektrolytisch Induzierte Keimbildung in Schmelzen Dargestellt anhand der Gerichteten Kristallisation von Fresnoit. Ph.D. Thesis, Friedrich-Schiller-Universität, Jena, Germany, 1997.
13. Keding, R.; Rüssel, C. Oriented glass-ceramics containing fresnoite prepared by electrochemical nucleation of a BaO-TiO_2-SiO_2-B_2O_3 melt. *J. Non-Cryst. Solids* **2000**, *278*, 7–12. [CrossRef]
14. Höche, T.; Keding, R.; Rüssel, C.; Hergt, R. Microstructural characterization of grain-oriented glass-ceramics in the system $Ba_2TiSi_2O_8$-SiO_2. *J. Mater. Sci.* **1999**, *34*, 195–208. [CrossRef]
15. Keding, R.; Rüssel, C. Electrochemical nucleation for the preparation of oriented glass ceramics. *J. Non-Cryst. Solids* **1997**, *219*, 136–141. [CrossRef]
16. Honma, T.; Komatsu, T.; Benino, Y. Patterning of c-axis-oriented $Ba_2TiX_2O_8$ (X = Si, Ge) crystal lines in glass by laser irradiation and their second-order optical nonlinearities. *J. Mater. Res.* **2008**, *23*, 885–888. [CrossRef]
17. Honma, T.; Ihara, R.; Benino, Y.; Sato, R.; Fujiwara, T.; Komatsu, T. Writing of crystal line patterns in glass by laser irradiation. *J. Non-Cryst. Solids* **2008**, *354*, 468–471. [CrossRef]
18. Wisniewski, W.; Nagel, M.; Völksch, G.; Rüssel, C. Electron Backscatter Diffraction of Fresnoite Crystals Grown from the Surface of a $2BaO_3 \cdot TiO_2 \cdot 3\ 2.75SiO_2$ Glass. *Cryst. Growth Des.* **2010**, *10*, 1414–1418. [CrossRef]
19. Ochi, Y.; Meguro, T.; Kakegawa, K. Orientated crystallization of fresnoite glass-ceramics by using a thermal gradient. *J. Eur. Ceram. Soc.* **2006**, *26*, 627–630. [CrossRef]
20. Patschger, M.; Wisniewski, W.; Rüssel, C. Piezoelectric glass-ceramics produced via oriented growth of $Sr_2TiSi_2O_8$ fresnoite: Thermal annealing of surface modified quenched glasses. *CrystEngComm* **2012**, *14*, 7368–7373. [CrossRef]
21. Müller, R.; Zanotto, E.D.; Fokin, V.M. Surface crystallization of silicate glasses: Nucleation sites and kinetics. *J. Non-Cryst. Solids* **2000**, *274*, 208–231. [CrossRef]
22. Reinsch, S.; Müller, R. Nucleation at silicate glass surfaces. In *Analysis of the Composition and Structure of Glass and Glass Ceramics*; Springer: Berlin, Germany, 1999; pp. 379–398.
23. Wisniewski, W.; Rüssel, C. Oriented surface nucleation in inorganic glasses—A review. *Prog. Mater. Sci.* **2021**, *118*, 100758. [CrossRef]
24. Wisniewski, W.; Saager, S.; Böbenroth, A.; Rüssel, C. Experimental evidence concerning the significant information depth of electron backscatter diffraction (EBSD). *Ultramicroscopy* **2017**, *173*, 1–9. [CrossRef] [PubMed]

25. Otto, K.; Wisniewski, W.; Rüssel, C. Growth mechanisms of surface crystallized diopside. *CrystEngComm* **2013**, *15*, 6381–6388. [CrossRef]
26. Wisniewski, W.; Otto, K.; Rüssel, C. Oriented Nucleation of Diopsode Crystals in Glass. *Cryst. Growth Des.* **2012**, *12*, 5035–5041. [CrossRef]
27. Tielemann, C.; Busch, R.; Reinsch, S.; Patzig, S.; Höche, T.; Avramov, I.; Müller, R. Oriented surface nucleation in diopside glass. *J. Non-Cryst. Solids* **2021**, *562*, 120661. [CrossRef]
28. Wisniewski, W.; Takano, K.; Takahashi, Y.; Fujiwara, T.; Rüssel, C. Microstructure of transparent strontium fresnoite glass-ceramics. *Sci. Rep.* **2015**, *5*, 9069. [CrossRef] [PubMed]
29. Wisniewski, W.; Patschger, M.; Murdzheva, S.; Thieme, C.; Russel, C. Oriented Nucleation of both Ge-Fresnoite and Benitoite/$BaGe_4O_9$ during the Surface Crystallisation of Glass Studied by Electron Backscatter Diffraction. *Sci. Rep.* **2016**, *6*, 20125. [CrossRef]
30. Wisniewski, W.; Bocker, C.; Kouli, M.; Nagel, M.; Rüssel, C. Surface crystallization of fresnoite from a glass studied by hot stage scanning electron microscopy and electron backscatter diffraction. *Cryst. Growth Des.* **2013**, *13*, 3794–3800. [CrossRef]
31. Wisniewski, W.; Döhler, F.; Rüssel, C. Oriented Nucleation and Crystal Growth of Ba-Fresnoite ($Ba_2TiSi_2O_8$) in 2 $BaO{\cdot}TiO_2{\cdot}2\ SiO_2$ Glasses with Additional SiO_2. *Cryst. Growth Des.* **2018**, *18*, 3202–3208. [CrossRef]
32. Kracker, M.; Zscheckel, T.; Thieme, C.; Thieme, K.; Höche, T.; Rüssel, C. Morphology, topography, and crystal rotation during surface crystallization of BaO/SrO/ZnO/SiO_2 glass. *CrystEngComm* **2019**, *21*, 1320–1328. [CrossRef]
33. Cabral, A.A.; Fokin, V.M.; Zanotto, E.D.; Chinaglia, C.R. Nanocrystallization of fresnoite glass. I. Nucleation and growth kinetics. *J. Non-Cryst. Solids* **2003**, *330*, 174–186. [CrossRef]
34. Rodrigues, A.M.; Rivas Mercury, J.M.; Leal, V.S.; Cabral, A.A. Isothermal and non-isothermal crystallization of a fresnoite glass. *J. Non-Cryst. Solids* **2013**, *362*, 114–119. [CrossRef]
35. Moore, P.B.; Louisnathan, S.J. The crystal structure of fresnoite, $Ba_2(TiO)Si_2O_7$. *Z. Krist. Cryst. Mater.* **1969**, *130*, 438–448.
36. FIZ Karlsruhe. ICSD (Inorganic Crystal Structure Database). Available online: https://icsd.products.fiz-karlsruhe.de/en/about/about-icsd (accessed on 31 July 2015).
37. D'Souza, A.S.; Pantano, C.G. Mechanisms for silanol formation on amorphous silica fracture surfaces. *J. Am. Ceram. Soc.* **1999**, *82*, 1289–1293. [CrossRef]
38. Olsen, D.A.; Osteraas, A.J. The Critical Surface Tension of Glass. *J. Phys. Chem.* **1964**, *68*, 2730–2732. [CrossRef]
39. Jebsen-Marwedel, H.; Brückner, R. *Glastechnische Fabrikationsfehler. "Pathologische" Ausnahmezustände des Werkstoffes Glas und Ihre Behebung; Eine Brücke Zwischen Wissenschaft Technologie und Praxis*; Springer: Berlin, Germany, 1980.
40. Diaz-Mora, N.; Zanotto, E.D.; Hergt, R.; Müller, R. Surface crystallization and texture in cordierite glasses. *J. Non-Cryst. Solids* **2000**, *273*, 81–93. [CrossRef]
41. Müller, R.; Reinsch, S. Viscous phase silicate processing. *Process. Approaches Ceram. Compos.* **2012**, *3*, 75–144.
42. Komatsu, T.; Honma, T. Laser patterning and growth mechanism of orientation designed crystals in oxide glasses: A review. *J. Solid State Chem.* **2019**, *275*, 210–222. [CrossRef]
43. Tielemann, C.; Reinsch, S.; Maaß, R.; Deubener, J.; Müller, R. Internal nucleation tendency and crystal surface energy obtained from bond energies and crystal lattice data. *J. Non-Cryst. Solids X* **2022**, *14*, 100093. [CrossRef]